Fast, three-dimensional super-resolution imaging of live cells

Sara A Jones[1,5], Sang-Hee Shim[1,5], Jiang He[2] & Xiaowei Zhuang[1,3,4]

We report super-resolution fluorescence imaging of live cells with high spatiotemporal resolution using stochastic optical reconstruction microscopy (STORM). By labeling proteins either directly or via SNAP tags with photoswitchable dyes, we obtained two-dimensional (2D) and 3D super-resolution images of living cells, using clathrin-coated pits and the transferrin cargo as model systems. Bright, fast-switching probes enabled us to achieve 2D imaging at spatial resolutions of ~25 nm and temporal resolutions as fast as 0.5 s. We also demonstrated live-cell 3D super-resolution imaging. We obtained 3D spatial resolution of ~30 nm in the lateral direction and ~50 nm in the axial direction at time resolutions as fast as 1–2 s with several independent snapshots. Using photoswitchable dyes with distinct emission wavelengths, we also demonstrated two-color 3D super-resolution imaging in live cells. These imaging capabilities open a new window for characterizing cellular structures in living cells at the ultrastructural level.

The development of super-resolution fluorescence microscopy has allowed the diffraction-limited resolution to be surpassed[1,2]. This advance typically has been achieved in two ways: (i) spatially modulating the fluorescence emission with patterned illumination as in the cases of stimulated emission depletion microscopy (STED or reversible saturable optical fluorescence transitions (RESOLFT))[1,3] and saturated structured illumination microscopy (SSIM)[4,5], or (ii) stochastically switching individual molecules on at different times as in the case of stochastic optical reconstruction microscopy (STORM), photoactivation localization microscopy (PALM) or fluorescence PALM (FPALM)[6–8]. The latter approach also requires high-precision localization of single molecules[9,10] and photoswitchable probes. These techniques have allowed biological structures to be imaged with resolution as high as ~20 nm. Recent demonstrations of super-resolution imaging in living cells, as exemplified by the video-rate STED imaging of synaptic vesicles in live neurons[11], have enabled the characterization of cellular dynamics with sub-diffraction-limit resolution.

Owing to the intrinsic trade-off between spatial and temporal resolutions, however, the image resolution achieved in live cells is substantially lower than that for fixed samples, for which the imaging speed is not a concern. The spatial resolution reported for the video-rate live-cell STED is ~60 nm in the lateral dimensions, threefold larger than what has been achieved on fixed cells[11]. A recent live-cell STED study reports ~150 nm axial resolution when imaging samples in the *x*-*z* plane[12]. Live-cell SIM has achieved ~10 Hz imaging speed in a wide field with a spatial resolution of ~100 nm in the lateral dimensions[13]. For the single-molecule-based imaging methods, such as PALM, FPALM or STORM, this trade-off arises from the requirement that a sufficiently large number of localizations need to be accumulated for each snapshot in order to define a structure with a desired spatial resolution. This requirement is best characterized by the Nyquist criterion which equates the image resolution to 2/(localization density)$^{1/D}$, where $D = 1$, 2, or 3 for one-dimensional (1D), 2D or 3D imaging, respectively[14]. Therefore, although photoactivation-facilitated high-density particle tracking has proven powerful for probing molecular motions in living cells[15–17], the Nyquist criterion has so far limited the spatial resolution of the single-molecule-based imaging methods to 40–70 nm in two dimensions with a 30–60 s time resolution[14,18], when imaging photoactivatable fluorescent proteins in live cells. Two-dimensional super-resolution imaging has also been performed in living cells with photoswitchable dyes[19–22], but the localization density has not been characterized in these cases, and thus the image resolution achieved is unclear. Because more localizations are inherently required to define a structure in three dimensions, it is expected that extending super-resolution imaging to three dimensions will further deteriorate the time resolution. Indeed, 3D super-resolution imaging has not yet been achieved for live cells with the single-molecule-based methods. These limitations have hindered the application of super-resolution fluorescence microscopy to the ultrastructural characterization of living cells.

Here we report 2D and 3D super-resolution imaging of live cells with high spatial and temporal resolutions using photoswitchable dyes. We achieved a Nyquist resolution of ~20 nm with a time resolution as high as 0.5 s for 2D STORM imaging. Moreover, we achieved 3D volumetric super-resolution imaging of live cells

[1]Department of Chemistry and Chemical Biology, Harvard University, Cambridge, Massachusetts, USA. [2]Department of Molecular and Cellular Biology, Harvard University, Cambridge, Massachusetts, USA. [3]Department of Physics, Harvard University, Cambridge, Massachusetts, USA. [4]Howard Hughes Medical Institute, Harvard University, Cambridge, Massachusetts, USA. [5]These authors contributed equally to this work. Correspondence should be addressed to X.Z. (zhuang@chemistry.harvard.edu) or S.-H.S. (shshim@fas.harvard.edu).

RECEIVED 1 SEPTEMBER 2010; ACCEPTED 15 APRIL 2011; PUBLISHED ONLINE 8 MAY 2011; DOI:10.1038/NMETH.1605

with an overall resolution of 30 nm in the *x*-*y* dimension and 50 nm in the *z* dimension at time resolutions as fast as 1–2 s, albeit with relatively few independent snapshots. We demonstrated these imaging capabilities not only for exogenously added molecules but also for intracellular proteins by delivering bright, fast-switching cyanine dyes into living cells and by using genetic fusion strategies to specifically label proteins with these probes. Additionally, we compared the 3D image resolutions achieved with six photoswitchable probes in live cells, including the photoswitchable cyanine dye, Alexa Fluor 647 (Alexa647), three cell-permeant photoswitchable dyes, Atto655, tetramethylrhodamine (TMR) and Oregon Green, and two photoactivatable Eos fluorescent protein derivatives, mEos2 and tdEos.

RESULTS

Model system for live-cell STORM

We used the clathrin-mediated endocytic machinery as a model system to test the above imaging capabilities. Clathrin-coated pits (CCPs) are responsible for the endocytosis of many cell-surface receptors and their cargos, among which transferrin is a classic example. Before live-cell imaging, we imaged the nanoscale morphology of CCPs and the enclosed transferrin clusters in fixed cells. For this purpose, we labeled transferrin and clathrin with photoswitchable probes using two strategies. The first was based on the activation properties of probes containing the photoswitchable dye Alexa647: we labeled transferrin directly with a photoswitchable dye pair, Alexa405-Alexa647, and immunolabeled clathrin with another dye pair, Cy3-Alexa647. In this scheme, we imaged the photoswitchable Alexa647 and distinguished the probes by the wavelength of light used to activate the dye pair[23,24]. In the second approach, we used two photoswitchable dyes with spectrally separable emission wavelengths: Alexa647 for clathrin labeling[25] and Alexa568 for transferrin labeling[19].

From among the various 3D STORM, PALM or FPALM approaches[26–30], we chose astigmatism imaging. In this approach, a cylindrical lens is inserted into the imaging path to render the image of each molecule elliptical; the centroid and ellipticity of the image are used to determine the lateral (*x* and *y*) and axial (*z*) coordinates of the molecule, respectively[26]. A 3D STORM image is then constructed from the *x*, *y* and *z* coordinates of all imaged molecules through iterative activation. We determined the localization precision of Alexa647 to be 7 nm in the *x*–*y* plane and 17 nm in the *z* dimension measured in s.d., which corresponds to 17 nm in the *x* and *y*, and 45 nm in the *z* dimension measured in full-width at half maximum (FWHM). The localization precision of Alexa568 was lower, 23 nm in the *x* and *y*, and 61 nm in the *z* dimension (FWHM) owing to its twofold reduction in photons per switching cycle as compared to Alexa647. The localization precision changed only slightly over the 300 nm imaging depth used in this work (Online Methods).

As expected, the STORM images had substantial resolution improvement compared to conventional images. In conventional images, the majority of transferrin and CCPs appeared as colocalized diffraction-limited puncta with no discernable morphological details (**Supplementary Fig. 1a**). In contrast, 3D STORM images showed transferrin as clusters with 50–80 nm width, enclosed by clathrin coats in the shape of a half-spherical shell of 100–200 nm in diameter (**Supplementary Fig. 1b–d**).

2D live-cell STORM with subsecond time resolution

First, we performed 2D imaging of transferrin clusters in live cells. We added Alexa405-Alexa647–labeled transferrin to cells that had been serum-starved to increase the surface density of transferrin receptors and thereby increase the number of receptors within each CCP. Cyanine dyes, such as Alexa647, switch off to a dark state by forming a thiol adduct in imaging buffer containing thiol[31]. We thus used beta-mercaptoethanol to support photoswitching and an oxygen scavenger system to reduce photobleaching, albeit in amounts smaller than what is typically used for fixed cell imaging to maintain cell health. To achieve fast imaging speeds, which directly depends on the switching rate of the probes, we used a 657-nm laser of up to 15 kW cm^{-2} (at the sample) to rapidly image and switch off individual Alexa647 molecules. To activate only an optically resolvable subset of molecules at any time, we used a weak 405-nm laser, typically two to four orders of magnitude less intense than the 657-nm laser. We kept both lasers on continuously to optimize the imaging speed[32]. We recorded STORM movies with 500-Hz camera frame rate. Our control experiments showed that neither the thiol- and oxygen scavenger system–containing imaging buffer nor the strong laser illumination exerted measurable effects on the cell morphology for at least 20 min (**Supplementary Fig. 2** and **Supplementary Movie 1**) or transferrin-uptake kinetics (**Supplementary Fig. 3**).

Under these conditions, individual Alexa647 molecules were switched off in about two camera frames on average, emitting an average of 3,500 photons per switching event (**Supplementary Fig. 4**). The fast switching kinetics of Alexa647 allowed us to record super-resolution images with high speed. We acquired a STORM image of transferrin clusters at room temperature (23 °C) over a wide field of view (**Fig. 1a**). A comparison with the conventional image revealed a substantial improvement in resolution (**Fig. 1b**). Wide-field imaging allowed us to acquire time series of many individual transferrin clusters, exemplified by two characteristic time series, each with six independent 0.5-s STORM snapshots (**Fig. 1c**). The cluster diameter and number of localizations in the clusters remained largely unchanged from snapshot to snapshot. Owing to the short snapshot duration (0.5 s), the observed size and shape of the cluster did not show substantial motion-blurring effects; analysis of data for many clusters revealed a similar cluster size distribution when compared to that obtained in fixed cells (**Supplementary Fig. 5a**,**b**).

For assessing the spatial resolution of these STORM snapshots, we note that the image resolution is limited not only by the localization precision of each probe molecule but also by the localization density in the structures. According to the Nyquist criterion, the average distance between neighboring localizations should be no more than half of the size of an object for the object to be resolvable. Therefore, a Nyquist resolution of 2/(localization density)$^{1/D}$ must also be considered when specifying the spatial resolution, in addition to the localization precision[14]. The measured cluster size and number of localizations in the cluster allowed us to determine the localization density for each cluster. Although each Alexa647 molecule could potentially give multiple localizations, we used the localization density to calculate the Nyquist resolution for the following two reasons. First, under our experimental conditions, the snapshot durations were shorter than or comparable to the average time between consecutive activation events of a single probe. Therefore, the localization density

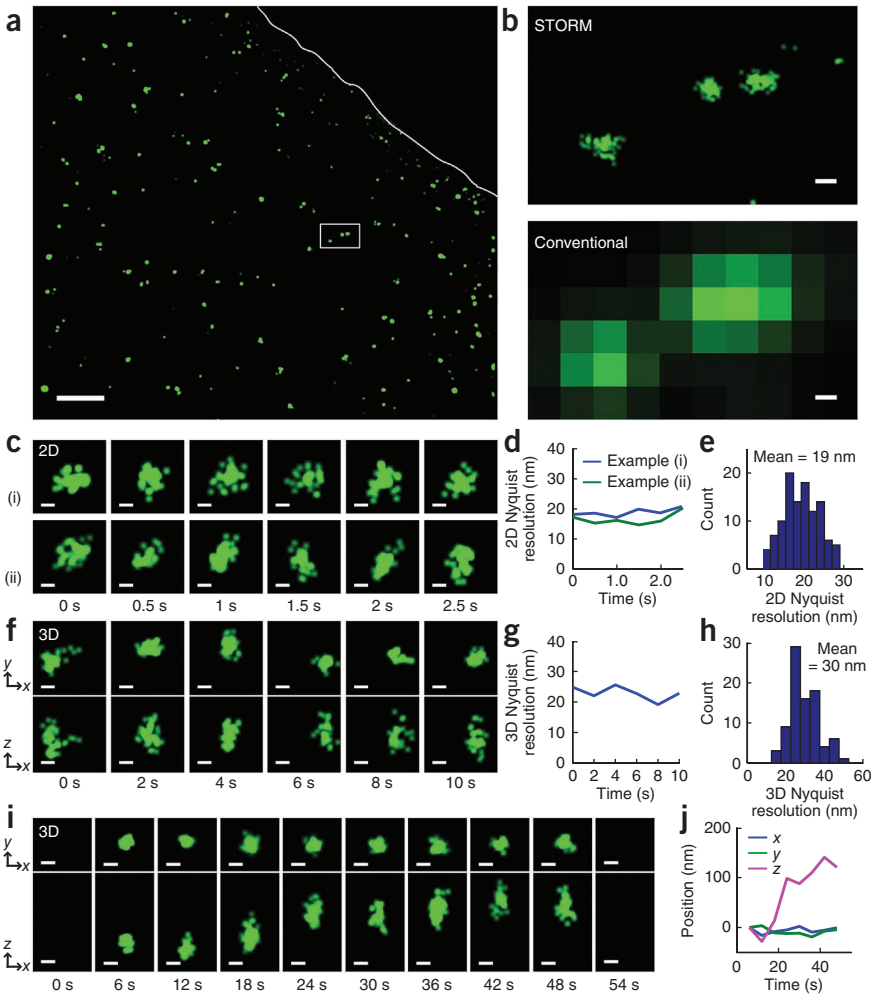

Figure 1 | STORM images of transferrin in live cells. (**a**) Wide-field 2D STORM image. Analysis was limited to inside the cell boundary, demarcated by the white line, owing to unreliable STORM localizations outside the cell caused by fluorescence background from diffusing transferring molecules. (**b**) Close-up 2D STORM (top) and conventional (bottom) images of the boxed region in **a**. (**c**) Examples of two transferrin clusters, each showing six consecutive 2D STORM snapshots (0.5 s per snapshot). (**d**) The 2D Nyquist resolution for the examples shown in **c**. (**e**) Histogram of Nyquist resolutions constructed from many individual transferrin clusters at 0.5-s time resolution. (**f**) Consecutive 3D STORM snapshots of a transferrin cluster (2 s per snapshot); *x-y* (top) and *x-z* (bottom) projections are shown. (**g**) The 3D Nyquist resolution derived from the snapshots in **f**. (**h**) Histogram of 3D Nyquist resolutions, constructed from many clusters at 2-s time resolution. (**i**) Images of a transferrin cluster at 6 s per snapshot at 34 °C showing its time evolution, starting from formation (6 s) to disappearance (54 s) upon internalization; *x-y* (top) and *x-z* (bottom) projections are shown. (**j**) The *x*, *y* and *z* coordinates of the centroid position of the transferrin cluster in **i**. Scale bars, 2 μm (**a**), 100 nm (**b**) and 50 nm (**c**,**f**,**i**). In all images and in other figures, the *z* axis points away from the glass substrate.

was comparable to the activated probe density in each snapshot. In all experiments throughout this work, the Nyquist resolution would change by 30% or less if the activated probe density was used for calculation. Second, transferrin receptors diffuse in CCPs. We measured a diffusion coefficient of 0.06 $\mu m^2\ s^{-1}$ for transferrin in the clusters, which is consistent with previous results[33]. Therefore, multiple localizations of the same moving probe can be included to sample the underlying cluster shape. A similar strategy has been used to map the bacterial cytoskeleton structure with live-cell super-resolution imaging[18]. For the 0.5-s STORM snapshots in the above examples, we determined the Nyquist resolution to be less than 20 nm (**Fig. 1d**). Analysis of many transferrin clusters recorded at 0.5-s time resolution yielded an average 2D Nyquist resolution of 19 nm (**Fig. 1e**). After convolution with the 17-nm localization precision (measured in FWHM), we obtained an overall resolution of 25 nm.

3D live-cell STORM

Most cellular structures have a 3D organization, and therefore 3D super-resolution imaging is required to resolve their ultrastructure. Considering that the localizations in this case are spread out not only in the lateral dimensions but also in the axial dimension, a larger number of localizations, and thus a longer imaging time, are needed to achieve a similar Nyquist resolution. Despite this requirement, the fast switching kinetics of Alexa647 allowed us to obtain 3D STORM images of a wide field of view with high speed. As an example, we show 3D STORM snapshots of a transferrin cluster obtained every 2 s, with a 3D Nyquist resolution of ~22 nm (**Fig. 1f,g**). Analysis of many transferrin clusters recorded at 2-s time resolution yielded a Nyquist resolution distribution averaged at 30 nm (**Fig. 1h**), which, when convolved with the localization precision, gave an overall resolution of 34 nm in *x-y* and 54 nm in *z* dimensions. Analysis of many clusters taken in live cells showed a similar cluster size distribution as that obtained in fixed cells, indicating a lack of substantial motion-blurring effects (**Supplementary Fig. 5a,c**). The overall imaging time was, however, relatively short for this high-speed imaging condition because of photobleaching of the probes and therefore insufficient to capture the internalization process of the transferrin cluster.

We thus reduced the activation laser intensity to decrease the on-switching rate of the probe and acquired 6-s snapshots for a longer period of time at 34 °C. Even at this time resolution and elevated temperature, the size distribution of the clusters showed minimal motion blurring, with the average cluster size comparable to that obtained at 0.5-s and 2-s resolution (**Supplementary Fig. 5d**). We captured the dynamics of a transferrin cluster, from formation to disappearance (**Fig. 1i**). The cluster formed at ~6 s, remained largely stationary in the lateral dimension as the *z* position increased considerably (**Fig. 1i,j**) and finally disappeared abruptly at ~50 s in a single snapshot. This rapid disappearance is unlikely due to photobleaching, which would result in a more gradual decrease in the localization number as different molecules photobleach stochastically at different times. Instead,

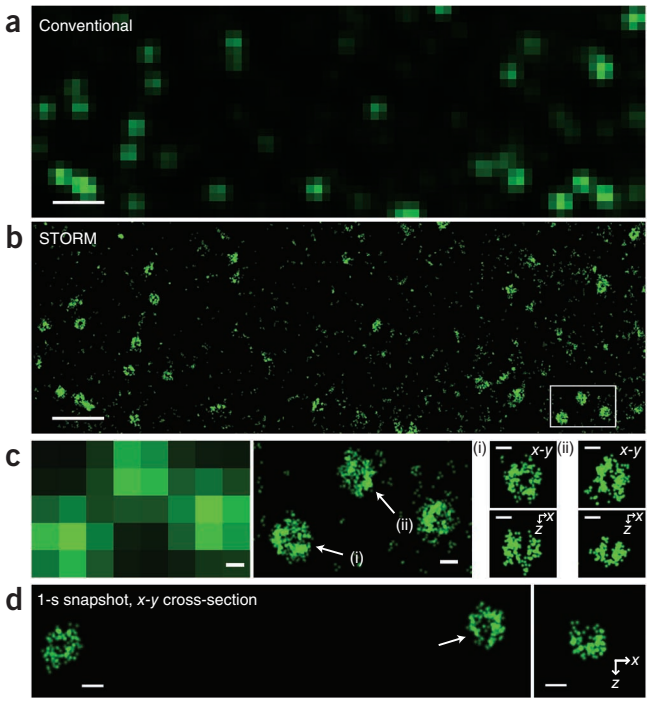

Figure 2 | 3D STORM images of CCPs labeled with photoswitchable cyanine dyes via a SNAP tag in live cells. (**a**) Conventional wide-field image of CCPs in a live cell. (**b**) A 3D STORM image of the same area taken in 30 s. Only *x-y* projection is shown. (**c**) Conventional (left) and 3D STORM (center; *x-y* projection) images of the boxed region in **b**. Cross-sections of CCPs at the indicated locations are shown on the right: *x-y* cross-section near the plasma membrane (top images) and *x-z* cross-section cutting through the middle of the CCP (bottom images). (**d**) A 3D STORM image taken in 1 s showing an *x-y* cross-section of two CCPs (left) and an *x-z* cross-section of the CCP indicated by the arrow. Scale bars, 1 μm (**a**,**b**) and 100 nm (**c**,**d**).

the sudden disappearance was likely due to internalization of the cluster given that endocytic vesicles often embark on rapid cytoskeleton-dependent movement immediately after internalization and thereby leave the shallow imaging field[34]. Supporting this notion, analysis of multiple clusters showed that the mean disappearance time was 72 ± 14 s, which is quantitatively comparable to the internalization time measured at 34 °C for transferrin using conventional imaging methods with the same buffer and temperature conditions (**Supplementary Fig. 3**).

3D live-cell STORM of intracellular proteins

In the above examples, we labeled proteins of interest directly with photoswitchable dyes before addition to live cells. Applying a similar labeling approach to intracellular proteins, such as clathrin, would be more challenging. Instead, we used the SNAP-tag technology[35] for specific clathrin labeling with Alexa647. To this end, we generated a construct encoding a SNAP tag and clathrin light chain (CLC) fusion and transfected cells with this construct. Then, using electroporation, we delivered the SNAP-reactive Alexa647 molecules (BG-Alexa647) into living cells. The distribution and dynamics of CCPs in cells expressing this dye-labeled fusion protein were similar to those expressing the previously validated EYFP-CLC fusion construct[34,36].

We first performed imaging experiments at room temperature with a relatively slow time resolution of 30 s using low 405-nm activation-light intensity (**Fig. 2**). Conventional images of the Alexa647-labeled clathrin showed the expected punctate pattern of CCPs, which appeared as diffraction-limited spots with no discernable structure (**Fig. 2a**,**c**). In contrast, live-cell 3D STORM images resolved the nanoscopic structure of CCPs (**Fig. 2b**,**c**). The *x-y* and *x-z* cross-sections of individual CCPs revealed the cup-like morphology of the clathrin coat (**Fig. 2c**). The average 3D Nyquist resolution of CCPs observed in an entire field of view was 24 nm, which gave an overall resolution of 29 nm in *x-y* and 51 nm in *z* dimensions after convolution with the localization precision of Alexa647 (**Supplementary Table 1**). The size distribution of CCPs determined from these 30-s snapshots was similar to the distribution determined from both the 10-s snapshots of live cells and the fixed cell images (**Supplementary Fig. 6**), indicating minimal motion-blurring effects, as expected from the slow CCP dynamics at room temperature.

Increasing the 405-nm activation intensity allowed us to improve the time resolution to as fast as 1 s while maintaining a similar Nyquist resolution at 32 nm (**Fig. 2d**). The observation of the nontrivial, cup-like shape of CCPs suggests that 3D STORM can indeed be used to resolve nanoscopic structures in live cells.

Approaches other than electroporation can be used to deliver dye molecules into living cells. We also obtained STORM images of CCPs in live cells by delivering BG-Alexa647 using a bead-loading method[37] (**Supplementary Fig. 7**).

Two-color 3D STORM in live cells

By adding Alexa568-labeled transferrin to cells expressing Alexa647-labeled SNAP-CLC fusion proteins, we obtained two-color 3D STORM images of transferrin and clathrin in live cells (**Fig. 3**). The 30-s STORM images allowed us to clearly discriminate transferrin and clathrin, which appeared as completely overlapping puncta in the conventional images (**Fig. 3a**,**b**). The morphology of the clathrin coat enclosing the transferrin cluster

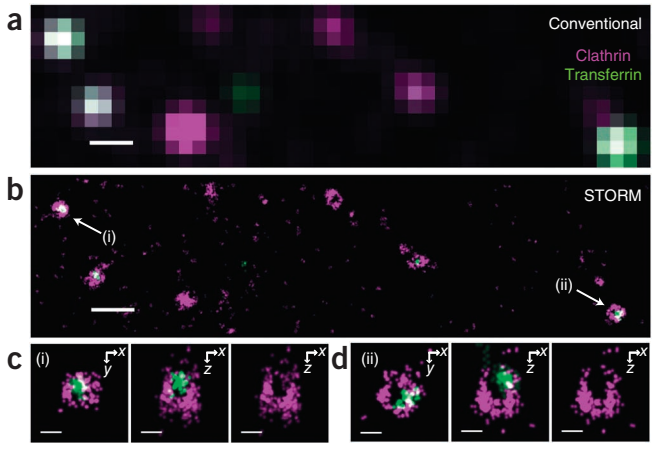

Figure 3 | Two-color 3D STORM images of CCPs and transferrin in live cells. (**a**) Conventional image of CCPs and transferrin in a live cell. CCPs were labeled with Alexa647 via a SNAP tag (magenta) and transferrin was directly labeled with Alexa568 (green). (**b**) A 3D STORM image *x-y* projection of the same area taken in 30 s. (**c**,**d**) STORM images of CCPs indicated in **b**: *x-y* cross-section near the plasma membrane (left), *x-z* cross-section cutting through the middle of the invaginating CCP (middle) and corresponding *x-z* cross-section of the clathrin channel only (right). Scale bars, 500 nm (**a**,**b**) and 100 nm (**c**,**d**).

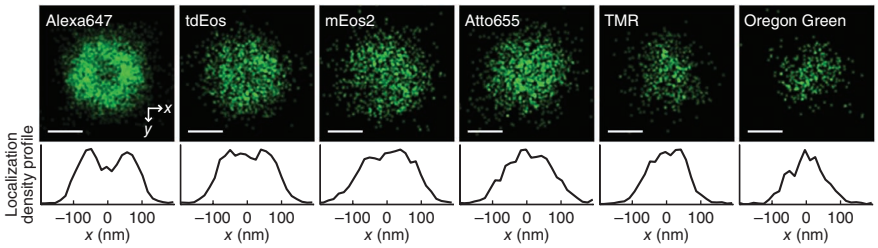

Figure 4 | Comparison of CCPs labeled with various probes. Composite CCPs were constructed by aligning the 3D center of mass of CCPs in an entire field of view for each probe. A portion of the field of view is displayed in **Figure 2b** for Alexa647 and in **Supplementary Figure 8** for tdEos, mEos2, Atto655, TMR and Oregon Green. The *x*-*y* cross-sections through the 3D center of the composite CCPs are shown (top). Scale bars, 100 nm. Localization density profiles along the *x* axis within a 75-nm wide stripe at the center of CCPs are also shown (bottom).

was resolved in this nanoscopic cellular structure (**Fig. 3b**–**d**). The resolution in the transferrin channel was lower than that of the single-color transferrin image taken with Alexa647 owing to the smaller number of photons detected from Alexa568 (~1,700 photons). The overall resolution was 40 nm in *x*-*y* and 70 nm in *z* dimensions in the transferrin channel. The resolution in the clathrin channel remained largely unchanged from the single-color cases described earlier.

Comparison with other photoswitchable probes

Given the requirement of live-cell delivery of the non-cell-permeant Alexa647, we next tested several additional photoswitchable probes for live cell super-resolution imaging and compared their performance with that of Alexa647. These probes include monomeric (m)Eos2 and tandem dimer (td)Eos, two of the brightest photoactivatable fluorescent proteins[14,38,39], and three cell-permeant photoswitchable dyes, Atto655, TMR and Oregon Green, which have been used previously for live-cell super-resolution imaging[14,20–22]. For imaging with Eos fluorescent proteins, we created a fusion protein of CLC and mEos2 or tdEos. For imaging with the organic dyes, we used the SNAP tag as described above for Alexa647. Among the SNAP-reactive substrates, we found BG-TMR and BG–Oregon Green to be cell-permeant and added them to the cells expressing SNAP-CLC directly. BG-Atto655 did not penetrate the cell membrane, and we delivered it into living cells by electroporation, as in the case of BG-Alexa647.

The 30-s 3D STORM snapshots of CCPs labeled with these probes are shown in **Supplementary Figure 8**. Among these probes, tdEos and mEos2 offered higher image quality than Atto655, TMR and Oregon Green. But because of the relatively small number of photons detected from individual mEos2 and tdEos molecules (~1,200 photons), the image resolution obtained with these probes was not as good as that with Alexa647. The overall resolution, considering both localization precision and density, was ~40 nm in *x*-*y* and ~80 nm in *z* dimensions for mEos2 and tdEos (**Supplementary Table 1**). As a result, the cup-like morphology of CCPs was no longer clearly resolved (**Supplementary Fig. 8a**,**b**). Although an interferometry approach can be used to increase the image resolution, the requirement to sandwich the sample between two closely opposing objectives makes it more difficult to implement for live cells[29]. Moreover, it is difficult to increase the imaging speed substantially because of the photophysical properties of these fluorescent proteins. Unlike Alexa647, which emitted a constant number of photons per switching cycle independent of the excitation light intensity (**Supplementary Fig. 4c**), the number of photons emitted by an Eos fluorescent protein before switching off decreased with the excitation intensity (**Supplementary Fig. 9a**). The light used to image the activated form of Eos also appeared to cause bleaching of the unactivated form (**Supplementary Fig. 9b**), reducing the localization density at high excitation intensity. These properties prevented the use of higher light intensity to achieve a faster imaging speed.

Compared to the two fluorescent proteins, the three photoswitchable dyes, Atto655, TMR and Oregon Green, additionally suffered from lower localization density, leading to an additional reduction in image resolution (**Supplementary Fig. 8c**–**e** and **Supplementary Table 1**). Because stronger illumination further reduced the number of attainable localizations, we could not improve the time resolution to beyond 30 s in these cases. For these probes with relatively small photon numbers, we also observed a moderately larger *z*-dimension variation in the localization precision (Online Methods).

To facilitate quantitative comparison, we constructed a composite image of CCPs for each of the six probes from CCP structures detected in an entire field of view. The *x*-*y* cross-sections of the composite CCP images and their density profiles along the *x* direction are shown in **Figure 4**. The composite image of the Alexa647-labeled CCPs shows a ring-like cross-section, as expected for the coated pits. Owing to the broad size distribution of CCPs, the thickness of the composite ring appeared wider than our image resolution. In contrast, the hollow center of the ring structure was not clearly revealed in the tdEos and mEos2 images, which instead exhibited a top-hat profile. The profiles of the Atto655, TMR and Oregon Green images, in particular the latter two, exhibited a Gaussian-like shape and did not resolve the CCP morphology.

DISCUSSION

To obtain high spatiotemporal resolution, several parameters must be considered. First, because the super-resolution image is reconstructed from localizations of individual molecules, the localization precision is a key determinant of the image resolution. Among the six photoswitchable probes we tested here, Alexa647 gave the highest photon output in each switching cycle, corresponding to a localization precision of 17 nm in *x*-*y* and 45 nm in *z* dimensions (FWHM), which was considerably higher than the photon output for tdEos, mEos2, Atto655, TMR and Oregon Green (**Supplementary Table 1**). For live-cell imaging, it is also important to consider how the movement of individual probe molecules in the structure may affect the localization precision. For example, under our experimental conditions, transferrin molecules diffused by ~20 nm during the 2-ms camera frame, which should have only a moderate effect on our image resolution. Another important factor in spatial resolution is the localization density. Based on the Nyquist criterion, a sufficient number of localizations is needed to define the structure with a desired resolution in each snapshot. As the total number of localizations is limited by the density of labels

on the structure of interest and the photoswitching properties of the probe molecules, the total number of snapshots attainable is limited. Although Alexa647-labeled structures tend to give more localizations as compared to other probes, the overall number of snapshots attainable per structure is still rather limited, especially for CCPs at the high spatial resolution described here. A future challenge is to identify probes with more switching cycles under live-cell imaging conditions for better characterization of ultrastructural dynamics.

To obtain high temporal resolution, the critical factor is the photoswitching rate of the probes. Alexa647 maintains a constant photon output independent of the excitation intensity. This property allowed us to switch Alexa647 molecules rapidly with high illumination intensity and to achieve a time resolution that is two orders of magnitude greater than previously reported for single-molecule–based super-resolution imaging in living cells. Given the trade-off between time resolution and overall imaging time, it is sometimes beneficial to reduce the time resolution for probing longer processes. Reducing the time resolution by decreasing the imaging laser intensity is, however, not always desirable because a slower off-switching rate may cause degradation of the localization precision, especially if the probe molecules diffuse inside the structure. Alternatively, the time resolution can be adjusted without the above concern by tuning the on-switching rate with the activation light intensity as demonstrated here.

Finally, the choice of probe is a balancing act between desired spatial and temporal resolutions, attainable localization density and ease of use. All six probes tested in this work provided subdiffraction image resolution in three dimensions. The fluorescent proteins and cell-permeant dyes have the advantage of allowing relatively easy labeling of live cells and, in the case of fluorescent proteins, lower nonspecific labeling background. But the superior brightness and faster switching kinetics of Alexa647 make it the probe of choice for imaging at very high spatiotemporal resolution. Because Alexa647 is a non-membrane-permeant dye, labeling intracellular proteins in living cells with this dye requires not only specific labeling chemistry for cellular proteins but also nontrivial live-cell delivery of the dye molecules. In addition to the SNAP-tag technology, a variety of other hybrid fusion systems can be used to link dye molecules to the protein of interest through a genetically fused peptide sequence or protein tag[20,21,40]. We demonstrated two different dye delivery approaches, electroporation and bead loading, for STORM imaging. In particular, electroporation combines both high efficiency and reproducibility. Nonetheless, it is still a relatively laborious approach and can cause cell-to-cell variation in labeling efficiency. Future development of cell-permeant cyanine dyes is desirable to enhance the versatility of these probes for live-cell super-resolution imaging.

Many subcellular structures have nanometer-scale dimensions. The characterization of many of these structures in fixed cells is subject to fixation artifacts, especially at the ultrastructural level. We thus expect the high-spatiotemporal-resolution imaging capabilities demonstrated here to substantially benefit ultrastructural characterizations in living cells.

METHODS

Methods and any associated references are available in the online version of the paper at http://www.nature.com/naturemethods/.

Note: Supplementary information is available on the Nature Methods website.

ACKNOWLEDGMENTS

We thank M. Davidson (Florida State University) and L. Looger (Janelia Farm) for Eos fluorescent protein plasmids. This work is supported in part by the US National Institutes of Health (to X.Z.) and a Collaborative Innovation Award (43667) from Howard Hughes Medical Institute. S.-H.S. is in part supported by the Mary Fieser fellowship. X.Z. receives support from the Howard Hughes Medical Institute.

AUTHOR CONTRIBUTIONS

X.Z. conceived of the project. S.A.J., S.-H.S. and X.Z. designed the experiments. S.A.J. and S.-H.S. performed all experiments and analysis. J.H. assisted with bead-loading experiments. S.A.J., S.-H.S. and X.Z. wrote the manuscript.

COMPETING FINANCIAL INTERESTS

The authors declare no competing financial interests.

Published online at http://www.nature.com/naturemethods/.
Reprints and permissions information is available online at http://www.nature.com/reprints/index.html.

1. Hell, S.W. Far-field optical nanoscopy. *Science* **316**, 1153–1158 (2007).
2. Huang, B., Babcock, H. & Zhuang, X. Breaking the diffraction barrier: super-resolution imaging of cells. *Cell* **143**, 1047–1058 (2010).
3. Klar, T.A. & Hell, S.W. Subdiffraction resolution in far-field fluorescence microscopy. *Opt. Lett.* **24**, 954–956 (1999).
4. Heintzmann, R., Jovin, T.M. & Cremer, C. Saturated patterned excitation microscopy—a concept for optical resolution improvement. *J. Opt. Soc. Am. A Opt. Image Sci. Vis.* **19**, 1599–1609 (2002).
5. Gustafsson, M.G.L. Nonlinear structured-illumination microscopy: wide-field fluorescence imaging with theoretically unlimited resolution. *Proc. Natl. Acad. Sci. USA* **102**, 13081–13086 (2005).
6. Rust, M.J., Bates, M. & Zhuang, X. Sub-diffraction-limit imaging by stochastic optical reconstruction microscopy (STORM). *Nat. Methods* **3**, 793–795 (2006).
7. Betzig, E. *et al.* Imaging intracellular fluorescent proteins at nanometer resolution. *Science* **313**, 1642–1645 (2006).
8. Hess, S.T., Girirajan, T.P. & Mason, M.D. Ultra-high resolution imaging by fluorescence photoactivation localization microscopy. *Biophys. J.* **91**, 4258–4272 (2006).
9. Thompson, R.E., Larson, D.R. & Webb, W.W. Precise nanometer localization analysis for individual fluorescent probes. *Biophys. J.* **82**, 2775–2783 (2002).
10. Yildiz, A. *et al.* Myosin V walks hand-over-hand: single fluorophore imaging with 1.5-nm localization. *Science* **300**, 2061–2065 (2003).
11. Westphal, V. *et al.* Video-rate far-field optical nanoscopy dissects synaptic vesicle movement. *Science* **320**, 246–249 (2008).
12. Hein, B., Willig, K.I. & Hell, S.W. Stimulated emission depletion (STED) nanoscopy of a fluorescent protein-labeled organelle inside a living cell. *Proc. Natl. Acad. Sci. USA* **105**, 14271–14276 (2008).
13. Kner, P., Chhun, B.B., Griffis, E.R., Winoto, L. & Gustafsson, M.G. Super-resolution video microscopy of live cells by structured illumination. *Nat. Methods* **6**, 339–342 (2009).
14. Shroff, H., Galbraith, C.G., Galbraith, J.A. & Betzig, E. Live-cell photoactivated localization microscopy of nanoscale adhesion dynamics. *Nat. Methods* **5**, 417–423 (2008).
15. Hess, S.T. *et al.* Dynamic clustered distribution of hemagglutinin resolved at 40 nm in living cell membranes discriminates between raft theories. *Proc. Natl. Acad. Sci. USA* **104**, 17370–17375 (2007).
16. Manley, S. *et al.* High-density mapping of single-molecule trajectories with photoactivated localization microscopy. *Nat. Methods* **5**, 155–157 (2008).
17. Subach, F.V. *et al.* Photoactivatable mCherry for high-resolution two-color fluorescence microscopy. *Nat. Methods* **6**, 153–159 (2009).
18. Biteen, J.S. *et al.* Super-resolution imaging in live *Caulobacter crescentus* cells using photoswitchable EYFP. *Nat. Methods* **5**, 947–949 (2008).
19. Heilemann, M., van de Linde, S., Mukherjee, A. & Sauer, M. Super-resolution imaging with small organic fluorophores. *Angew. Chem. Int. Edn. Engl.* **48**, 6903–6908 (2009).
20. Wombacher, R. *et al.* Live-cell super-resolution imaging with trimethoprim conjugates. *Nat. Methods* **7**, 717–719 (2010).
21. Testa, I. *et al.* Multicolor fluorescence nanoscopy in fixed and living cells by exciting conventional fluorophores with a single wavelength. *Biophys. J.* **99**, 2686–2694 (2010).
22. Klein, T. *et al.* Live-cell dSTORM with SNAP-tag fusion proteins. *Nat. Methods* **8**, 7–9 (2011).

23. Bates, M., Huang, B., Dempsey, G.T. & Zhuang, X. Multicolor super-resolution imaging with photo-switchable fluorescent probes. *Science* **317**, 1749–1753 (2007).
24. Huang, B., Jones, S.A., Brandenburg, B. & Zhuang, X. Whole-cell 3D STORM reveals interactions between cellular structures with nanometer-scale resolution. *Nat. Methods* **5**, 1047–1052 (2008).
25. Zhuang, X. Nano-imaging with Storm. *Nat. Photonics* **3**, 365–367 (2009).
26. Huang, B., Wang, W., Bates, M. & Zhuang, X. Three-dimensional super-resolution imaging by stochastic optical reconstruction microscopy. *Science* **319**, 810–813 (2008).
27. Juette, M.F. *et al.* Three-dimensional sub-100 nm resolution fluorescence microscopy of thick samples. *Nat. Methods* **5**, 527–529 (2008).
28. Pavani, S.R.P. *et al.* Three-dimensional, single-molecule fluorescence imaging beyond the diffraction limit by using a double-helix point spread function. *Proc. Natl. Acad. Sci. USA* **106**, 2995–2999 (2009).
29. Shtengel, G. *et al.* Interferometric fluorescent super-resolution microscopy resolves 3D cellular ultrastructure. *Proc. Natl. Acad. Sci. USA* **106**, 3125–3130 (2009).
30. Tang, J., Akerboom, J., Vaziri, A., Looger, L.L. & Shank, C.V. Near-isotropic 3D optical nanoscopy with photon-limited chromophores. *Proc. Natl. Acad. Sci. USA* **107**, 10068–10073 (2010).
31. Dempsey, G.T. *et al.* Photoswitching mechanism of cyanine dyes. *J. Am. Chem. Soc.* **131**, 18192–18193 (2009).
32. Egner, A. *et al.* Fluorescence nanoscopy in whole cells by asynchronous localization of photoswitching emitters. *Biophys. J.* **93**, 3285–3290 (2007).
33. Sako, Y. & Kusumi, A. Barriers for lateral diffusion of transferrin receptor in the plasma membrane as characterized by receptor dragging by laser tweezers: fence versus tether. *J. Cell Biol.* **129**, 1559–1574 (1995).
34. Rust, M.J., Lakadamyali, M., Zhang, F. & Zhuang, X. Assembly of endocytic machinery around individual influenza viruses during viral entry. *Nat. Struct. Mol. Biol.* **11**, 567–573 (2004).
35. Keppler, A. *et al.* A general method for the covalent labeling of fusion proteins with small molecules *in vivo*. *Nat. Biotechnol.* **21**, 86–89 (2003).
36. Gaidarov, I., Santini, F., Warren, R.A. & Keen, J.H. Spatial control of coated-pit dynamics in living cells. *Nat. Cell Biol.* **1**, 1–7 (1999).
37. McNeil, P.L. & Warder, E. Glass beads load macromolecules into living cells. *J. Cell Sci.* **88**, 669–678 (1987).
38. McKinney, S.A., Murphy, C.S., Hazelwood, K.L., Davidson, M.W. & Looger, L.L. A bright and photostable photoconvertible fluorescent protein. *Nat. Methods* **6**, 131–133 (2009).
39. Wiedenmann, J. *et al.* EosFP, a fluorescent marker protein with UV-inducible green-to-red fluorescence conversion. *Proc. Natl. Acad. Sci. USA* **101**, 15905–15910 (2004).
40. Fernandez-Suarez, M. & Ting, A.Y. Fluorescent probes for super-resolution imaging in living cells. *Nat. Rev. Mol. Cell Biol.* **9**, 929–943 (2008).

ONLINE METHODS

Cell culture. BS-C-1 cells (CCL-26; American Type Culture Collection (ATCC)), an African Green monkey kidney epithelial cell line, were maintained in a 5% CO_2 atmosphere at 37 °C in Eagle modified minimum essential medium (ATCC), supplemented with 10% fetal bovine serum (Invitrogen). Cells were passaged every 2–3 d and maintained for up to 15 passages. For imaging, cells were plated into 8-well chambered coverglasses (LabTek-II; Nalgene Nunc) cleaned previously with 1 M potassium hydroxide, at a density of ~16,000–30,000 cells per well depending on the experiment.

Plasmid construction. To generate *CLC-Eos* plasmids, sequences encoding mEos2 (gift of L. Looger and M. Davidson) or tdEos (gift of M. Davidson) were fused to the 5′ or 3′ end of sequences encoding mouse CLC version A, respectively. mEos2 was digested out of the pmEos2-N vector using AgeI (5′ end) and NotI (3′ end) and ligated into a similarly digested, previously described pEYFP-mLCa vector[34,36]. An intermediate tdEos-C1 plasmid was generated by exchanging *tdEos* for *EYFP* in pEYFP-C1 (5′ end, NheI and 3′ end, EcoRI; Clontech) and subsequently *mLCa* was inserted between KpnI (5′ end) and ApaI (3′ end) restriction sites. To generate the pEYFP-CLC-SNAP vector, *SNAP26m* was amplified from the pSNAP-tag(m) vector (New England Biolabs) with added XhoI (5′ end) and EcoRI (3′ end) sites, digested and then ligated into a similarly digested pEYFP-mLCa vector. The pSNAP-CLC-SNAP vector was generated by replacing the *EYFP* in the pEYFP-CLC-SNAP vector with *SNAP26m*, a PCR product from pSNAP-tag(m), with added AgeI (5′ end) and NotI (3′ end) restriction sites. We engineered the *EYFP-CLC-SNAP* construct for easier identification of transfected cells with the EYFP fluorescence signal and the *SNAP-CLC-SNAP* construct with two SNAP tags for increased labeling density. The distribution and dynamics of CCPs in cells expressing CLC-mEos2 and tdEos-CLC fusion proteins, and in cells expressing EYFP-CLC-SNAP and SNAP-CLC-SNAP fusion proteins were similar to those observed in cells expressing EYFP-CLC, a fusion protein that has been previously validated to be functionally intact[34,36].

Transfection. Trypsinized cells were transiently transfected with a Nucleofector Device (Lonza) using Cell Line Nucleofector Kit V and program X-001. Transfected cells were then plated into 8-well chambered coverglasses and used for experiments 24–40 h after transfection. For labeling SNAP-tagged proteins with dyes delivered into live cells by electroporation, cells were first nucleofected with a combination of pSNAP-CLC-SNAP and pEYFP-CLC-SNAP constructs (3:1 ratio) for increasing label density and for easy identification of transfected cells. For two-color imaging with Alexa568-transferrin only pSNAP-CLC-SNAP was used to avoid spectral overlap. Transfected cells were then plated into a culture flask. Because nucleofection is a solution-based technique, once tagged-protein expression was maximal (after ~18–24 h) cells were trypsinized again and nucleofected a second time with program T-030 in the presence of 100 µM BG-Alexa647 (BG-Surface Alexa Fluor 647; New England Biolabs) or BG-Atto655 (gift from New England Biolabs) for dye delivery. Cells were then replated onto 8-well chambered coverglasses, the medium was changed after ~4 h, and cells were imaged ~10–20 h after plating. For labeling with cell-permeant dyes, ~24 h after nucleofection with pSNAP-CLC-SNAP alone, cells were incubated for 30 min in 5 µm BG-TMR-Star or BG-OregonGreen (New England Biolabs) diluted in culture medium[21,22]. Cells were rinsed three times and allowed to recover at 37 °C in the absence of dye for 1–2 h before imaging. Increasing either the labeling concentration or incubation time did not result in a greater extent of labeling. For dye delivery with the bead-loading method, cells were loaded with 425–600 µm acid-washed glass beads (Sigma Aldrich) as previously described[37] in 50 µM BG-Alexa647, and allowed to recover at 37 °C for 30–60 min before imaging.

Immunostaining. Approximately 24 h after plating cells were serum-starved in DMEM with high glucose and no phenol red (Invitrogen) for 60 min. Alexa568-labeled transferrin (5 µg ml^{-1}; Invitrogen) or Alexa405-Alexa647-labeled transferrin (20 µg ml^{-1}) was either cold-bound for 10 min on ice followed by 37 °C incubation for 2 min, or bound at room temperature (23 °C) for 2 min without temperature shift, before fixation with 4% paraformaldehyde (Electron Microscopy Sciences). Both transferrin incubation conditions gave similar results. Immunofluorescence was performed as previously described using antibodies to clathrin heavy chain (ab21679, Abcam or MA1-065, Thermo Scientific) and corresponding secondary antibody (Jackson Immunoresearch)[24,41]. For Alexa405-Alexa647-transferrin, a Cy3-Alexa647 secondary antibody was used, and for Alexa568-transferrin, an Alexa405-Alexa647-labeled secondary antibody was used.

Live-cell imaging. For imaging Alexa647, cells were rinsed twice in serum-free DMEM and transferred to the microscope stage. Imaging buffer was then prepared with DMEM (high glucose, no phenol red; Invitrogen) or DMEMgfp (Evrogen) supplemented with 2% glucose, 6.7% of 1 M HEPES (pH 8.0), 0.5% beta-mercaptoethanol (Sigma) and an oxygen-scavenging system (0.5 mg ml^{-1} glucose oxidase and 40 µg ml^{-1} catalase) was added immediately before image acquisition. mEos2, tdEos, TMR, Oregon Green and Atto655 probes were imaged in DMEM as previously described[14,20,21]. Among these five probes, mEos2, tdEos and Atto655 gave higher imaging quality than TMR and Oregon Green. We tested whether adding the oxygen-scavenger system and beta-mercaptoethanol could improve the image quality for these probes but did not find them to be helpful in these cases. For imaging transferrin, cells were incubated in serum-free DMEM for 30–60 min at 37 °C. After cells were transferred to the microscope stage, Alexa405-Alexa647-transferrin or Alexa568-transferrin was added *in situ*, left for 1 min and then diluted by six times with imaging buffer immediately before image acquisition.

To correct for sample drift, 100-nm polystyrene fluorescent beads (Fluospheres, red fluorescent; Invitrogen) were affixed to the chambered coverglass by heating at 100 °C as fiducial markers[42]. The chambers were allowed to cool and rinsed extensively with water before cells were plated. Imaging experiments were performed at room temperature or at 34 °C in the transferrin internalization experiment. The latter condition allowed for more rapid internalization such that the internalization process could be recorded within our imaging window.

Optical setup and image acquisition. All STORM experiments were performed on an Olympus IX71 inverted optical microscope. Six laser beams at wavelengths of 657 nm (RCL-300-656;

doi:10.1038/nmeth.1605

Crystalaser), 561 nm (Sapphire 561-250; Coherent), 532 nm (GCL-200-l; Crystalaser), 514 nm (Sapphire 514-50; Coherent), 460 nm (Sapphire 460-10; Coherent) and 405 nm (CUBE 405-50C; Coherent) were individually controlled by mechanical shutters (Uniblitz LS6T2; Vincent Associates) and an acousto-optic tunable filter (AOTF PCAOM NI VIS; Crystal Technology). All laser lines were combined and coupled into an optical fiber (Oz Optics), and the fiber output was collimated and focused on the back focal plane of a high-numerical-aperture (NA) oil-immersion objective (100× UPlanSApo, NA1.4; Olympus). Because CCPs are primarily located at the plasma membrane, we used a total internal reflection fluorescence or highly oblique incidence imaging geometry to reduce background fluorescence, but note that such geometry is not a general requirement for 3D STORM, which allows wide-field imaging with a depth of a few micrometers[24]. The fluorescence emission was collected by the same objective and imaged onto a back-illuminated electron-multiplying charge-coupled device (EMCCD) camera (iXON DU-860 or iXON DU-897; Andor). To stabilize the focus during data acquisition, an 830 nm fiber-coupled diode laser (LPS-830-FC; Thorlabs) was introduced into the microscope in a separate objective-type total internal reflection path. The reflected infrared beam from the coverglass-water interface was directed to a quadrant photodiode. The position readout of the quadrant photodiode provided feedback to a piezo objective positioner (Nano-F100; MadCity Labs), keeping the focal drift to less than 20 nm.

For single-color imaging of Alexa647, the probes were activated by the 405-nm laser and the activated Alexa647 molecules were imaged with a 657-nm laser. The excitation beams were reflected by a dichroic long-pass mirror (T660LPXR; Chroma) and the fluorescence emission was filtered with a band-pass filter (ET705/72m; Chroma). For live-cell imaging, 657-nm intensity at ≤15 kW cm^{-2} (at the sample) was used to record movies at a frame rate of 500 Hz (iXON DU-860). The intensity of the 405 nm activation laser (2–4 orders of magnitude weaker than the 657-nm light) was ramped up to compensate for loss of dyes owing to photobleaching when needed.

Atto655 was imaged with a 657-nm laser as in the case of Alexa647 but at a lower intensity (~6 kW cm^{-2}). For imaging of tdEos, mEos2 and TMR, the probes were imaged with a 561 nm laser (~5 kW cm^{-2}). The laser was reflected by a dichroic long-pass mirror (Di01-R561; Semrock) and the fluorescence emission was filtered with a band-pass filter (FF01-617/73; Chroma). Increasing the imaging laser intensity caused a considerable reduction in the number of localizations attainable and consequently a lower imaging quality. Like in the case of Alexa647 imaging, the probes were activated by the 405-nm laser, the intensity of which was ramped up to compensate for loss of dyes owing to photobleaching when needed. OregonGreen was imaged with a 514-nm beam (~1 kW cm^{-2}, maximum power available on our setup) reflected by a dichroic long-pass filter (FD520-Di02; Semrock) and the fluorescence was filtered by a band-pass filter (FF01-578/105; Semrock). The fluorescence images were obtained at 100–150 Hz.

For two-color imaging of the Alexa405-Alexa647 and Cy3-Alexa647 probes, we used an alternating activation sequence of 405-nm and 532-nm laser pulses for activating the Alexa405-Alexa647 and Cy3-Alexa647 probes, respectively[23]. The activated Alexa647 molecules were again imaged with a 657-nm laser. For two-color imaging of Alexa647 and Alexa568, two imaging beams (561 nm and 657 nm) and an activation beam (405 nm) were reflected by a custom-designed polychroic mirror (z405/561/657rpc; Chroma). Fluorescence emissions from Alexa647 and Alexa568 were separated by a 630-nm long-pass dichroic mounted on a commercial beamsplitting device (Dual-View; Photometrics). The short-wavelength channel was filtered with a bandpass filter (FF01-607/70; Semrock) for Alexa568. The long-wavelength channel was filtered with a bandpass filter (ET705/72m; Chroma) for Alexa647. In addition to the bandpass filters, a double-notch filter (NF01-568/647; Semrock) was added before the Dual-View to block the two excitation beams. The two images were each imaged onto 128 × 128 pixels in the EMCCD camera (iXON DU-860) running at 500Hz.

For 3D localization, a cylindrical lens with a focal length of 50 cm (for imaging with the iXON DU-860 camera) or 100 cm (for imaging with the iXON DU-897 camera) was inserted into the imaging optical path[26].

Image analysis. STORM images were generated using similar methods as previously described[26]. Briefly, images of individual molecules were identified and fit to an elliptical Gaussian function to obtain the centroid position coordinates (x_0 and y_0) and the Gaussian widths (d_x and d_y). The lateral position of the molecule was determined as x_0 and y_0, and the z position was calculated from d_x and d_y using a calibration curve independently determined by imaging 100-nm fluorescent bead (Tetraspeck; Invitrogen) on a coverglass while scanning in the z direction. The z position was then corrected for refractive index mismatch between glass and the imaging medium as previously described[24].

We considered other factors that could potentially make single-molecule images appear elliptical, such as the polarized emission of dyes with fixed dipole orientations, which could contribute to the z localization error. In our experiments, individual molecular images did not appear elliptical in the absence of the cylindrical lens and the measured residual ellipticity resulted in a Δz of 17 nm, which is well within our z-localization precision for all probes, indicating that the z-dependent astigmatism was the primary source of ellipticity.

Sample drift during the image acquisition in both lateral and axial directions was measured and corrected by two means as described previously[26]: (i) correlation function of the image itself for fixed-cell images; and (ii) traces of fiducial markers for long (>50 s) time series of live cells. Sample drift was negligible in live-cell images of shorter durations.

In two-color images of immunostained samples in **Supplementary Figure 1a–c**, where the probes were distinguished by the activation wavelength, the color cross-talk resulting from nonspecific activation or false activation was subtracted as described previously[23]. For two-color imaging of Alexa647 and Alexa568, the two STORM images were aligned by a third-order polynomial warping map in three dimensions obtained from calibration images of 100-nm Tetraspeck fluorescent beads. The residual alignment error was ~7 nm in x-y and ~15 nm in z dimensions.

Cell autofluorescence and out-of-focus or nonspecifically bound fluorescent molecules give background in the STORM images, which appeared as scattered localizations at low local densities. To remove the background noise, STORM images were filtered according to the local density of localizations. This treatment has

the same function as background subtraction in conventional fluorescence imaging. Briefly, for each localization, the number of neighboring localizations was counted within a circular (for 2D images) or a spherical (for 3D images) region of a finite diameter of 50–80 nm to determine the local density of this localization. Localizations with local densities less than a specified cutoff value (2–5 per unit area or volume) were removed. As an example, we compared STORM images of a CCP containing transferrin with and without density filtering (**Supplementary Fig. 10**). The image with density filtering is also shown in **Supplementary Figure 1c**. Subsequent analyses on size distribution and Nyquist resolution were performed on the density-filtered images.

To determine the localization precision of the six probes, we imaged fluorescent beads with a diameter of 100 nm. Localization accuracy of each probe was calculated from the FWHM of localization distribution of individual beads. We adjusted the imaging laser intensity such that the average photon number detected from the beads per imaging frame was identical to the average photon number of the probe per switching cycle. This method was used because the photoactivable mEos2 and tdEos produce 1–2 localization per molecule, which does not allow the measurement of localization precision from multiple localizations of the same molecules. For photoswitchable probes with multiple cycles, such as Alexa647, multiple localizations obtained from a single molecule can be used to determine the localization instead, which yielded similar results as the bead measurements. In the text and **Supplementary Table 1**, we report the average localization precision over the 300 nm imaging depth. We found that, for all seven probes studied here, the *x*-*y* localization precision changed only slightly with the *z* position and that the measured values in all *z* ranges were within 20% of the average value. The *z* localization precision of the brighter probes, Alexa647 and Alexa568, also varied only slightly (within 13% of the average value for Alexa647 and within 20% for Alexa568). For the probes with relatively low photon numbers, such as mEos2, tdEos, Atto655, TMR and Oregon Green, the variation of the *z* localization precision was more prominent: at $z = 0$, 100, 200 and 300 nm, the localization precisions were 74%, 81%, 107%, and 138% of the average value, respectively. Because most of the structures of interest (transferrin clusters and CCPs) were within the range of $z = 0$–200 nm, the variation in localization precision was even smaller.

To quantitatively compare spatial resolution of different probes, we reported convolved resolutions computed as $((\text{localization precision})^2 + (\text{Nyquist resolution})^2)^{1/2}$. When localization precision and Nyquist resolution differ substantially, the resolution is limited by the larger of the two. When the localization accuracy and Nyquist resolution are comparable, both factors contribute substantially and the convolved resolution provides a good measure of the overall resolution.

41. Lakadamyali, M., Rust, M.J. & Zhuang, X. Ligands for clathrin-mediated endocytosis are differentially sorted into distinct populations of early endosomes. *Cell* **124**, 997–1009 (2006).
42. Nugent-Glandorf, L. & Perkins, T.T. Measuring 0.1-nm motion in 1 ms in an optical microscope with differential back-focal-plane detection. *Opt. Lett.* **29**, 2611–2613 (2004).

doi:10.1038/nmeth.1605